Plasma Structure Decay Rates in the Equatorial Ionosphere are Strongly Coupled by Turbulence

M F Ivarsen[1,2], J-P St-Maurice[2,3], J Park[4,5], J Klenzing J[6], Y Jin[1], and W Lee[4,5]

[1]Department of Physics, University of Oslo, Oslo, Norway
[2]Department of Physics and Engineering Physics, University of Saskatchewan, Saskatoon, Saskatchewan, Canada
[4]Korea Astronomy and Space Science Institute, Daejeon, South Korea
[5]Department of Astronomy and Space Science, Korea University of Science and Technology, Daejeon, South Korea
[3]Department of Physics and Astronomy, University of Western Ontario, London, Ontario, Canada
[6]Goddard Space Flight Center, National Aeronautics and Space Administration, Greenbelt, MD, United States

Key Points:

- Turbulence forces equatorial irregularities to decay with a scale-independent rate
- Equatorial irregularities of scale-sizes between 500 m and 75 km are not dissipating by chemical recombination or perfect ambipolar diffusion
- Equatorial plasma irregularities exhibit a characteristic decay time of approximately 1.4 hours

Corresponding author: Magnus F Ivarsen, `m.f.ivarsen@fys.uio.no`

Abstract

Equatorial plasma irregularities in the ionospheric F-region proliferate after sunset, causing the most apparent radio scintillation “hot-spot” in geospace. These irregularities are caused by plasma instabilities, and appear mostly in the form of under-densities that rise up from the F-region’s bottomside. After an irregularity production peak at sunset, the amplitude of the resulting turbulence decays with time. Analyzing a large database of plasma irregularity spectra observed by one of the European Space Agency’s Swarm satellites, we have applied a novel but conceptually simple statistical analysis to the data, finding in the process that post-sunset turbulence in the F-region tends to decay with a uniform, scale-independent rate at night, thereby confirming and extending the results from earlier case studies. Our results should be of utility for large-scale space weather modelling efforts that are unable to resolve turbulent effects.

1 Introduction

The equatorial ionosphere is an area of our Earth’s space environment where the geomagnetic field is nearly horizontal and is, as a result, the birthplace of several interesting electro-hydrodynamic instabilities after sunset. These emerge from the large-scale generalized Rayleigh-Taylor instability (Kelley, 1989). In the evening sector of the topside F-region, localized depletions, or ‘bubbles’, of plasma are therefore routinely observed (Woodman & Hoz, 1976; Heelis, 2004; Kil, 2015). Having formed in the bottomside F-region, large scale bubbles evolve non-linearly while rising upward (Kil & Heelis, 1998; Eccles et al., 2015). Smaller scale structures are then seen to proliferate on the edges of said bubbles, where steep plasma gradients create favorable conditions for irregularity production (Hysell & Kudeki, 2004). Alongside the depletions, *enhancements*, or ’blobs’, also exist in the topside F-region equatorial ionosphere. Like bubbles, blobs are also located in the evening sector and, like bubbles, carry with them plasma irregularities over a wide range of scales (Oya et al., 1986; Park et al., 2003; Le et al., 2003). At the smaller scales, such irregularities in plasma density cause signal refraction and hence scintillation in satellite communication transmissions (Yeh & Liu, 1982; Basu & Basu, 1985).

The dataset used in the present study is a collection of *in-situ* observations of equatorial plasma bubbles and attendant smaller-scale equatorial irregularities. We make no distinction between clearly recognizable bubbles, blobs, or turbulent plasma observations in general. The useful data are a collection of irregularity spectra, which themselves are Fourier components belonging to turbulent plasma processes. We subject these spectra to a conceptually simple statistical analysis; we aggregate spectral power across 128 frequencies, binned by solar local time (LT) at the time of observation.

By definition, a power spectrum quantifies the distribution of fluctuation power across the (temporal or spatial) scales in which the sampled quantity fluctuates (Stoica & Moses, 2005). Exploiting this quality, PSD analysis is frequently applied to in-situ ionospheric observations of plasma density bubbles (Kelley et al., 1982; Rino et al., 2016), high-latitude turbulence (Mounir et al., 1991), as well as in the larger plasma environment of Earth (Borovsky, 2012). The PSD of ionospheric plasma irregularities is often approximated by a power law of the form

$$P(f) \propto f^{-\eta}, \tag{1}$$

where η is a real-valued exponent, referred to as the spectral index, and f represents frequency (convertible to spatial wavenumber by an assumption of stationary plasma from the spacecraft point of view). The exponent η has been the subject of many studies of equatorial plasma irregularities (e.g., Dyson et al., 1974; Rino et al., 1981; Kelley & McClure, 1981; Kil & Heelis, 1998). Steepening of this spectral index is proportional to the decay in fluctuation power with increasing wavenumber, and has been characterized in equatorial plasma numerous times in the literature (e.g., LaBelle et al., 1986; Hysell et al., 1994). The decay rate as a function of wavenumber is a manifestation of the active nonlinear distribution of power between wavenumbers, whose nature is a key property of turbulence (Kolmogorov, 1941).

Structured plasmas produce a signal in *in-situ* density time-series. Into this turbulent signal is embedded various forms of non-linear wavenumber interactions. It is not just influenced by the power growth from plasma instabilities, but can also describe irregularity dissipation (Vickrey & Kelley, 1982; Mounir et al., 1991; Ivarsen et al., 2019). For instance, dissipation due to ambipolar diffusion has been inferred to cause observable spectral steepening (Kivanc & Heelis, 1998; Ivarsen, St-Maurice, et al., 2021), where power decreases markedly with increasing wavenumber below some critical scale.

Owing to diffusive processes, plasma irregularity dissipation is invariably associated with a characteristic *structure lifetime*, which quantifies the ensuing temporal exponential decay (Vickrey & Kelley, 1982; Ivarsen, Jin, et al., 2021). A study by Hysell and Kelley (1997) investigated the structure lifetimes of decaying equatorial plasma irregularities around local midnight. The authors examined two consecutive orbits made by the AE-E satellite, which had a very low orbital inclination, at times enabling it to effectively orbit along the magnetic equator. The two orbits in question fortuitously did so, observing roughly the same plasma structures on both orbits. The authors exploited this fact to examine the decay in power across a range of wavevectors, during the course of 101 minutes. Hysell and Kelley (1997) found all wavevectors between 80 m and 64 km to decay at roughly the same rate, exhibiting a plasma structure lifetime around 1.4 hour.

A study contemporary to the previously mentioned, Kil and Heelis (1998) likewise investigated the temporal evolution of equatorial F-region plasma, also using data from the AE-E satellite. The authors of that study applied power spectral density analysis to the *in-situ* density measurements, and made a statistical foray into the spectral indices, or slopes, of the measured irregularity spectra. Kil and Heelis (1998) found that small-scale irregularities grow rapidly around sunset, before decaying shortly thereafter. The authors did not explicitly show a scale-independent decay of power, but concluded that power decays across all wavevectors around local midnight.

In the present study, we perform a simple but intriguing statistical analysis of equatorial F-region plasma irregularities, measured by a Swarm satellite. We sort turbulent spectra by the solar local time of their observation and examine the decay in power with increasing LT. Earth's rotation is the cause of this diurnal variable, and we consider it to simply denote the passage of time in a co-rotating frame. By fitting exponential curves to PSD as a function of LT, we estimate the e-folding time of decaying density irregularities at night in the equatorial region.

2 Methodology

The Swarm mission consists of three polar-orbiting satellites with a very high inclination (Friis-Christensen et al., 2006). This means that the satellites' orbits are primarily oriented north-south geographically, and the orbits can thus be perpendicular to the magnetic equator. In Figure 1a) we show the orbit of Swarm A at around 00:55 UT on 25 October 2014, in a plot showing magnetic latitude on the y-axis (using the Solar Magnetic coordinate system Hapgood, 1992) and LT along the x-axis. The *geographic* equator is shown with a blue line, while a shaded gray region shows the dark ionosphere at an altitude of 110 km.

As alluded to, at the equator the angle between the spacecraft trajectory and Earth's magnetic field lines can be parallel for a polar orbiting satellite. It is, however, usually oblique (see, e.g., Nakanishi et al., 2014, Figure 13). We must nevertheless consider this angle explicitly, and so we shall denote it by α; the full 3D angle between a vector pointing along the spacecraft trajectory and that of Earth's magnetic field, the latter estimated using the IGRF model (Alken et al., 2021). Figure 2a–b) illustrates the situation; when

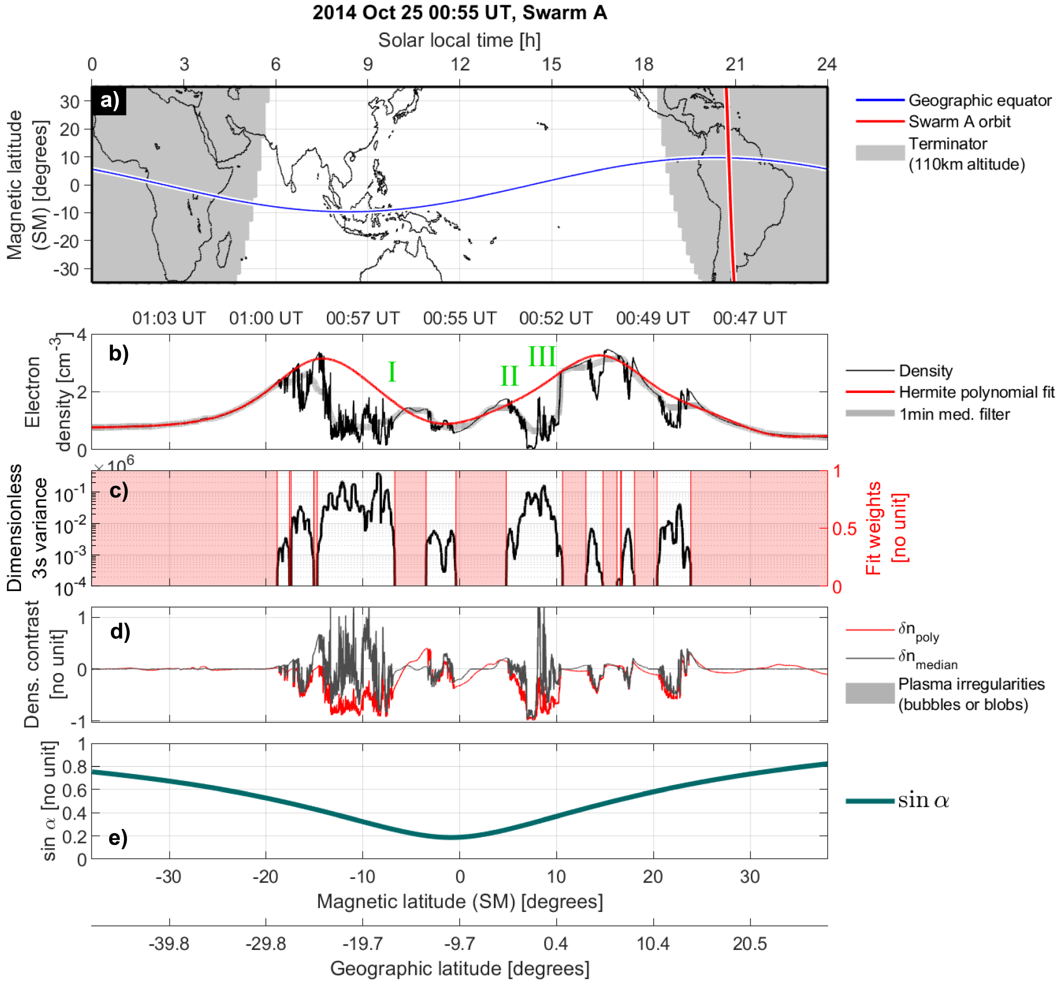

Figure 1. 25 October 2014, around 01:00 UT, Swarm A crossed the equator. Panel a) shows the orbit in local time (x) magnetic latitude (y) coordinates in red line, with the geographic equator in blue line. A shaded grey region indicates darkness in the E-region. Panel b) shows the observed plasma density (black), a Hermite polynomial fit (red), and a one-minute median filter applied to the density (grey). Panel c) shows the 3-second density variance in black, and the resulting fit weights (0 or 1) in shaded red area. The relative plasma density fluctuations δn is shown in gray and red line in Panel d). The angle between spacecraft velocity vector and Earth's magnetic field is shown in dark green line in panel e). The geographic and geomagnetic latitudes of the orbit are displayed on two x-axes below panel e). The three Roman numerals posted in panel b) refer to the panels of Figure 2.

$\alpha > 0$ the spacecraft velocity v_{sc} can be decomposed into a field-parallel ($v_{\parallel}$) and field-perpendicular ($v_{\perp}$) component. We assume the structures to be strongly magnetic field-aligned and therefore ignore the former while expressing the latter as

$$v_{\perp} = v_{sc} \sin \alpha. \tag{2}$$

Consequently, the rate at which the spacecraft traverses plasma *field-perpendicularly* gives the α-adjusted perpendicular scale size,

$$L_{\perp} = \frac{v_{sc} \sin \alpha}{f}, \tag{3}$$

where f denotes sampling frequency. Figure 2c plots $L_{\perp}$ for three selected frequencies. As $\sin \alpha$ approaches zero (orbit parallel to Earth's magnetic field lines) $L_{\perp}$ gets arbitrarily small, and the spacecraft runs the risk of resolving temporal waves, nullifying the hypothesis of plasma being stationary with respect to the spacecraft. We impose a threshold value of α that it must make an angle greater than 10° against Earth's magnetic field, which corresponds to $v_{\perp} \approx 1.3$ km/s. This threshold can also protect our results from the artefacts reported by Song et al. (2022).

It follows that when α is relatively small (but not too small) an orbiting spacecraft will effectively sample field-perpendicular irregularities at much smaller scale-sizes than the nominal sampling frequency would imply. The effective sampling frequency then becomes,

$$f_{\alpha} = \frac{f}{\sin \alpha}. \tag{4}$$

The consequences of this effective mapping between sampling frequency and *in-situ* spatial scale are understudied, but similar calculations were proposed by Kelley et al. (2003). The topic deserves to be revisited in a future paper.

The central observable used in the present study is the plasma density, $n(t)$, from the Advanced Plasma Density by the EFI instrument (Knudsen et al., 2017). With a sampling rate of 16 Hz (yielding a Nyquist frequency of 8 Hz). With Eq. (4), the effective Nyquist frequency becomes 16 Hz when $\alpha = 30^{\circ}$ – the average value of α in our dataset. The smallest field-perpendicular scale-sizes available in the data are consequently reduced to just under 500 m (see Figure S1 in the Supporting Information).

As is standard in many studies of plasma irregularities, we likewise quantify the *relative* fluctuations in density,

$$\delta n(t) = \frac{n(t)}{\bar{n}(t)} - 1, \tag{5}$$

where $\bar{n}(t)$ represents the ambient (undisturbed) density. We estimate $\bar{n}(t)$ using two techniques. One is by fitting a Hermite polynomial to the slowly varying equatorial plasma density, applying the reciprocal moving 3-second variance as weights in the fitting scheme. This way, orbital segments where the variance is high (implying the presence of irregularities) are not considered as representative of the ambient density. Second, as a more conventional way of calculating the density contrast, we estimate $\bar{n}(t)$ using a simple moving one-minute median filter.

To witness the two methods in action, see panel b) of Figure 1. Here, we show in thin black line the measured density, while a one-minute median filter is shown through a thick gray line, and the Hermite polynomial is shown with a red line. A density fluctuation time-series (Eq. 5) can consequently be constructed by division by one of the two estimated background density estimates. This being stated, while the Hermite polynomial evidently succeeds in building a slowly moving ambient density devoid of disturbances, neither method can provide a reliable ambient density inside bubble – that would require the measurement of a plasma density that no longer exists.

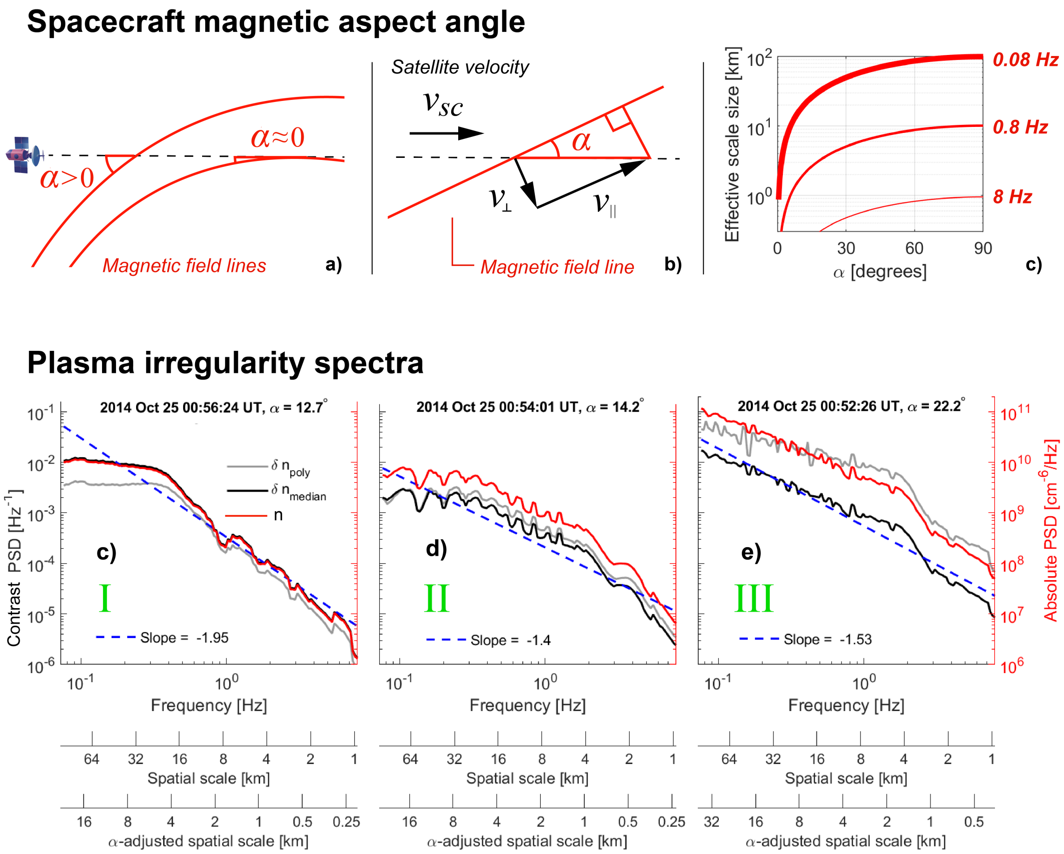

Figure 2. Panel a): the geometry of a spacecraft orbiting obliquely against Earth's magnetic field lines near the magnetic equator, making an angle α against the field-line. Panel b): the spacecraft velocity vector (v_{sc}), and its field-parallel and field-perpendicular components ($v_{\|}$ and $v_{\perp}$). Note that even though the sketch is 2-dimensional, we explicitly calculate the full 3D-angle. Panel c): Eq. (3) for three selected frequencies, as a function of α. Panels c–d) show example irregularity spectra that are subject to a statistical analysis in the present paper. The three panels show spectra calculated at denoted by green Roman numerals in Figure 1. The two density contrast spectra are shown in black and gray, while an absolute density spectrum is shown in red. Nominal and α-adjusted spatial scale (Eq. 3) are indicated along the two lower x-axes.

The relative plasma density fluctuations δn are shown in Figure 1d), a dark gray line representing the result of using a one-minute median filter, while a red line represents the result of using the Hermite polynomial to approach the relative fluctuations. We subjected these two time-series (as well as the absolute density) to a running PSD analysis with a cadence of 1 s. Each spectrum uses one minute segments, meaning that we calculate irregularity spectra with considerable overlap. After applying a Hann window to each 60 s segment, we computed averaged periodograms to calculate a logarithmically spaced PSD at 128 frequencies (Tröbs & Heinzel, 2006). This procedure is described in detail in Ivarsen, Jin, et al. (2021) and Ivarsen, St-Maurice, et al. (2021).

In Figure 2c–d) we show three sample spectra, calculated for the time-stamps marked with green Roman numerals in Figure 1b). We plot power spectral density against sampling frequency, with the relative density (contrast) spectra in terms of the median smoothing in black and the polynomial smoothing in gray (left y-axis). The absolute density spectrum is shown in red (right y-axis), in each panel. The lower x-axes give the conventional inferred scale size ($L = v_{sc}/f$), as well as the α-adjusted scale size (Eq. 3). The value of α as measured for each spectrum is indicated. We observe that all three spectra (black, grey, and red) agree appreciably, with slight variations in slope that are attributable to their difference in metric. In what follows, we aggregate some 2 million spectra such as those presented in Figure 2c–d), which are systematically classified according to the methods outlined above. In addition to the mentioned α-criterium, additional criteria for an irregularity spectrum to be identified and calculated include that $|\delta n|$ should be greater than at least 5 %, that the running 6 s density fluctuations variance should exceed 10^4, and the absolute density should exceed 5000 cm^{-3}.

3 Results

We processed an aggregate of some 25,000 equatorial night-time crossings made by Swarm A between 2014 and 2022, with the majority of the observations being made prior to 2020. Swarm B was excluded, as it is orbiting around at an altitude 50 km higher than Swarm A (around one scale height), and we excluded Swarm C, as that satellite orbits in tandem with Swarm A, and may observe largely the same structures as Swarm A. Based on the 25,000 selected orbits, we identified some 2 million irregularity spectra with the method outlined in the previous section. We then binned all observations by LT and by effective frequency (Eq. 4) to create composite information about the irregularities and their spectra.

Panels a) and b) in Figure 3 show the overall absolute density variance, σ_{RMS}, and the distribution of of irregularity spectra respectively, with both quantities binned by LT. In Panel b), we observe a steady rise in irregularity occurrence towards 04h, contrary to the maximum growth rates which peak just after sunset. The reason for this 04h peak is that bubbles tend to break up and spread out over a larger region of space as they decay, causing a larger number of spectra to be flagged as irregularities post-midnight compared to pre-midnight (see Figure S2 in the Supporting Information for a typical post-midnight crossing of the equator).

In panel a) of Figure 3, a straight green line shows the result of an exponential fit of the form

$$\sigma_{RMS} = \sigma_0 \, e^{-2t/\tau}, \tag{6}$$

where σ_0 and τ are (positive) fitting parameters calculated through a linear least-squares minimization applied to the logarithm of the median values, and t is the solar local time. We should mention here that equatorial F-region plasma tends to exhibit a horizontal west-east drift velocity (Purslow, 1958; Skinner et al., 1958). However, this drift does not show significant variations with respect to solar cycle, geomagnetic activity, or season (Woodman, 1972; Fejer et al., 1981). In Figure 3 (and the next figure to come) we could adjust the local times by the effect of this west-east plasma drift, but the correction has minimal impact on the results, and we abstain from making the adjustment.

The decay parameter $\tau = 1.52 \pm 0.27$ hours in Figure 3a), with error margins denoting the 95-percentile confidence interval (3-sigma) of the fit, indicate the e-folding time of the σ_{RMS} quantity with respect to LT, assuming an exponential decay in plasma irregularity amplitude after the sunset production peak. This value is consistent with the 1.4 h decay rate found by Hysell and Kelley (1997). Moreover, it is, as we shall demonstrate, largely independent of irregularity scale size. This decay rate is likewise relatively stable across different seasons (not shown), but displays a moderate dependency on geomagnetic activity, with geomagnetically disturbed conditions being associated with a slower decay until around 02h LT (see Figure S4 in the Supporting Information).

The rest of the panels in Figure 3 show the same binning procedure used for σ_{RMS} applied this time to the power spectral density in 16 selected α-adjusted frequencies between 0.2 Hz and 16 Hz (the effective Nyquist frequency, see Figure S1 in the Support-

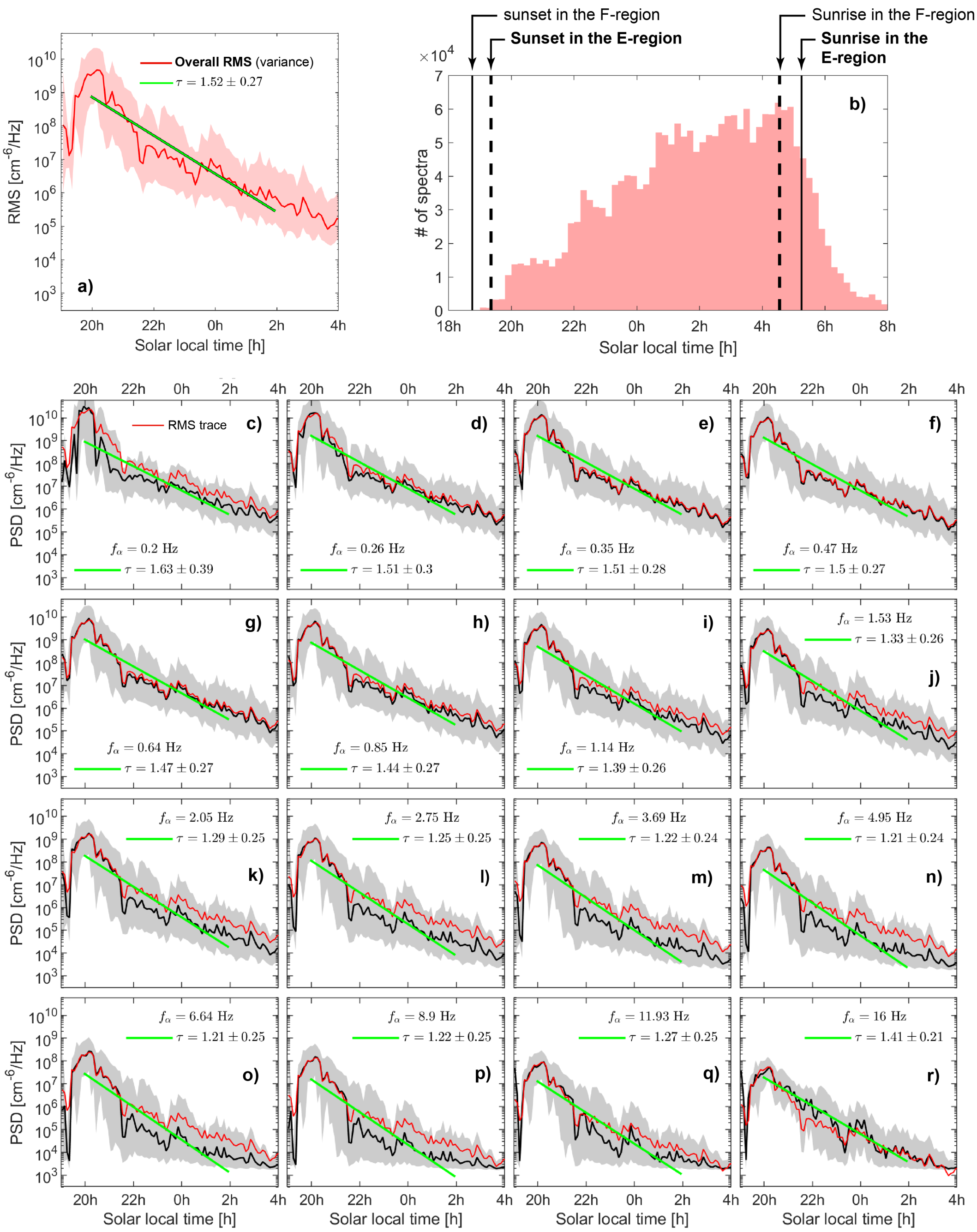

Figure 3. Overall absolute density variance (RMS) binned by solar local time (panel a). Number of spectra observed per local time bin, with various solar terminators indicated (panel b). Binned median power across 16 frequencies, with frequency indicated (panels c–r). Each of the 16 panels shows median PSD in black (shaded gray region showing upper- and lower- quartile distributions), with the trace of the overall RMS data shown in a thin red line. Exponential fits (Eq. 6) are shown in green, with structure lifetimes τ indicated. For a version of this figure based on relative density (contrast) spectra, see the Figure S3 in the Supporting Information.

ing Information). Panels c–r) of Figure 3 consequently show the median power in each local time bin (with a gray shaded area indicating upper- and lower- quartile distributions). A thin red line gives the trace of the overall RMS curve, multiplied by a constant number that changes with increasing frequency. That constant is selected so as to equalize the area under the σ_{RMS}- and the PSD-curve,leaving the shape of the shifted curve intact.

The agreement between the shifted σ_{RMS} and the PSD is remarkable between 0.26 Hz and 0.85, which happens to be where most of the wave energy is found. This is no accident in view of the following construct, where we Fourier analyze the variations in n_i when considering the RMS variations:

$$\sigma^2_{RMS} = \frac{1}{N}\sum_{i=1}^{N}\left[n_i(x_i) - \overline{n(\overline{x})}\right]^2 = \frac{1}{N}\left[n_0 - \overline{n(\overline{x})} + \sum_{k>0} n_k \cos(kx_i)\right]^2 \approx \frac{1}{2}\frac{\sum_{k>0} n_k^2}{N} \quad (7)$$

In these expressions, we take N x_i-samples (duration, 1 minute) and explicitly state that the average density is taken over the average x value for the interval. Secondly, we drop temporal variations, as explained in Section 2. We then assume that the $k = 0$ term in the Fourier series is equal to $\overline{n}$. Finally, we assume that the cosine terms oscillate strongly over the interval so that we replace the sum of the cosines by 0 and the sum of the squares of the cosines by 1/2. Thus, if the dominant wave-numbers all decrease in the same way as a function of LT, the RMS must mimic this decrease. This has to mean that, statistically speaking, the dominant wave numbers obey Eq. (1) with a single exponent η at all LT.

To estimate the decay individually for each α-adjusted frequency, and prove the above conjecture, we present the result of a fit through Eq. (6) for the PSD as a function of LT, for each individual frequency f_α. In Figure 3, τ, a value twice the e-folding time, is indicated in each panel. Note that while Figure 3 uses absolute density spectra, we have also repeated the procedure with the density contrast data, with similar results (see Figure S3 in the Supporting Information and Figure 4 below).

As a general summary of the data, we can state that the PSD decreases at roughly the same rate after the sunset peak, with a decay rate that fluctuates between 1.2 h and 1.6 h. This decay parameter is largely independent of frequency, and agrees well with the determination made by Hysell and Kelley (1997). This being stated, there are intriguing small variations in the spectral slope and decay rate as a function of frequency. These will be discussed in the next section.

4 Discussion

Figure 4 offers a different way to present our results by displaying the decay rates, τ, as a function of wavenumber $k = 2\pi/L = 2\pi f/(v_{sc}\sin\alpha)$ for all frequencies f. We remind the reader that $v_{sc}\sin\alpha$ denotes the component of the spacecraft velocity that is perpendicular to the geomagnetic field and that L is the spatial scale of irregularities. The thick green (absolute density) and blue (density contrast) lines give the post-sunset structure lifetimes, with shaded regions denoting the 95 percentile error margins of the underlying exponential fits. There is a tendency for faster decay times at intermediate frequencies and a longer decay time at the highest frequency (500 m scale), that also matches the decay of the largest structures. While real, it can be seen that the decay rate differences remain small, with less than a 20% excursion between extremes in spite of a frequency range that changes by nearly *two orders of magnitude*.

To illustrate the scale-dependent response in decay times that would be associated with ambipolar diffusion we also show the plasma diffusion lifetime based on the equation

$$\tau(k) = (k^2 D_a)^{-1}, \quad (8)$$

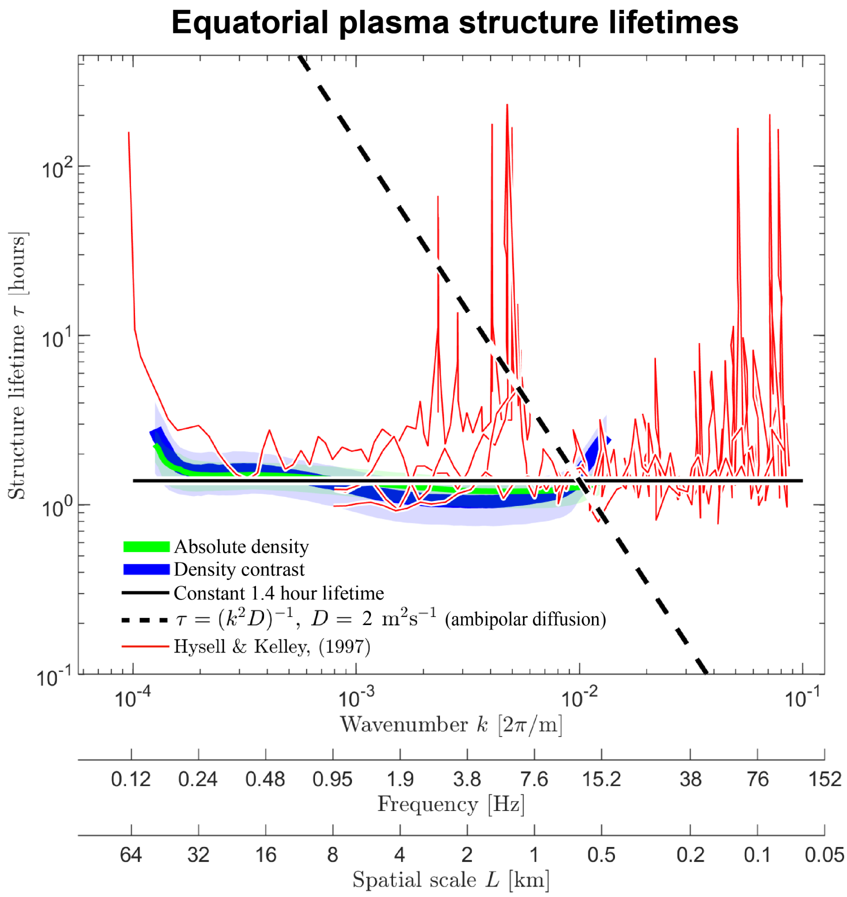

Figure 4. Exponential decay in all frequencies post-sunset (green and blue). Shaded blue and green areas indicate the 95-percent confidence intervals of the exponential fits. The results from Hysell and Kelley (1997) are plotted with four, thin red lines, representing four different measurements from the AE-E satellite. A power law fit (Eq. 8) is shown in thick dashed black line, while a constant 1.4 h lifetime is shown with a thick black line. The jump made by the blue curve at around 500 m scale-size could be due to noise, since the absolute plasma density (the denominator in Eq. 5) pre-sunrise is is extremely low).

where D_a is the ambipolar diffusion coefficient that can be found for example in Vickrey and Kelley (1982) and can be approximated with the formula

$$D_a = \frac{K_b T_e}{m_i} \frac{\nu_e}{\Omega_e \Omega_i}, \tag{9}$$

where K_b is the Boltzman constant, T_e is the electron temperature, m_i the ion mass, ν_e the electron collision frequency and Ω_e and Ω_i are the electron and ion gyrofrequencies respectively (Moisan & Pelletier, 2012). Eq. (8) is plotted with a thick dashed black line in Figure 4. In stark contrast, a thick solid black line shows a constant decay rate of 1.4 hours. Lastly, four thin red lines give the structure lifetimes estimated by Hysell and Kelley (1997), for four different iterations by the instrumentation on board the AE-E satellite. Notably, comparing the green and blue data with the thin red lines in Figure 4), the statistical results of the present paper are entirely consistent with the estimates by Hysell and Kelley (1997), with a decay rate of around 1.4 h for a similar satellite altitude as that of the AE-E satellite.

As pointed out by Hysell and Kelley (1997), a scale-independent decay post-sunset implies that equatorial plasma irregularities (for the most part bubbles) decay with the stochastic description of their structures intact. This will happen if cascading, through mode-coupling, transfers energy from larger scales to smaller ones, scales that then transfer energy to even smaller scales. If the structures decay all at the same rate, this means that the energy received at one scale is transferred back to the next scale at the same rate as it comes in. In that case, Hysell and Kelley (1997) have shown that the decay rate, τ, of previously excited structures has to be given by the condition

$$\tau \sum_{\mathbf{k}} |n_{\mathbf{k}}|^2 = D \sum_{\mathbf{k}} k^2 |n_{\mathbf{k}}|^2 \tag{10}$$

Using an ingenious heuristic model of turbulence, Hysell and Kelley (1997) have then found that the diffusion coefficient was approximately given by

$$D = \tau \frac{\ln(2k_1/k_0)}{k_1 k_2} \tag{11}$$

where the various k_i were associated with important wavelength regimes and τ was the observed decay rate of the structures. The intriguing part of this result was that the diffusion coefficient thus inferred was essentially the ambipolar diffusion coefficient for the altitude under consideration.

The retrieval of a local ambipolar diffusion coefficient may not be coincidental. Our argument as to why the local ambipolar diffusion is recovered is as follows: the large structures give energy to the next smaller structures at a given rate, and cascading carries this transfer of information down to a scale where ambipolar diffusion will become *more rapid* than the rate at which the structures receive energy through turbulent cascade. The onset of this rapid diffusion will determine the end point of the cascading as well as the rate at which the overall structures decay over the cascading interval. Although convincing, this description, with the quoted numbers, is generalized and not specific to case studies; Hysell and Kelley (1997)'s spectra exhibited scale-independent decay down to 80 m (red data in Figure 4).

5 Conclusion

We have analyzed some 25,000 equatorial crossings made by the Swarm A satellite during roughly ten years of operation, and applied a PSD analysis to the Swarm Advanced Plasma Density dataset. We have aggregated the power spectra, sorting by solar local time and frequency, before adjusting the instrument's sampling frequency by the (3D) angle between spacecraft velocity and ambient magnetic field lines (see Eqs. 2–4 and Figure 2).

Figures 3 and 4 show that, after the sunset production peak, equatorial density irregularities tend to decay with a characteristic lifetime that is largely independent of spatial scale, and in line with the only previous estimate (Hysell & Kelley, 1997).

A constant and regular structure lifetime of around 1.4 hours for equatorial plasma irregularities may have important consequences for research into climatological models for the purposes of space weather forecasting, with the overarching goal of mitigating the adverse effects of radio scintillations. After all, the decay rate regulates the degree to which irregularities proliferate during the equatorial night. For scales reaching up to 75 km, no wavevector gains more power than it receives until the local ambipolar diffusion rate is obtained. That rate evaluated for structures near the end of the turbulent cascade is what determines the rate at which the entire turbulent structure decays. This is in stark contrast with the classical ambipolar diffusion regime, which depends very strongly on spatial scales.

The relatively slow rate at which chemical recombination proceeds (Su et al., 2006) is exceeded by turbulent cascade, and so we expect chemical recombination rates not to be valid for the dissipation of < 75 km turbulence present in equatorial plasma bubbles. Large-scale models typically do not resolve this turbulence, and rely on instability growth rates when predicting climatologies. For the same reason, such models typically rely on decay rates that are based on expectations for chemical recombination. Our study provides a useful correction to this practice, offering a stepping stone to bridge the gap between observations (of turbulence) and the treatment of turbulent phenomena by large-scale modeling efforts.

Open Research

Data from the European Space Agency's Swarm mission can accessed at `https://swarm-diss.eo.esa.int/`

Acknowledgments

This work is a part of LIPS (the Lifetimes of Ionospheric Plasma Structures) project at the University of Oslo, and is supported in part by Research Council of Norway (RCN) grant 324859. The authors are grateful to L Clausen, H. Kil, and V. Eccles. YJ acknowledges funding from the European Research Council (ERC) under the European Union's Horizon 2020 research and innovation programme (ERC Consolidator Grant agreement No. 866357, POLAR-4DSpace). Part of this research has been performed under the 4DSpace Strategic Research Initiative at the University of Oslo.

References

Alken, P., Thébault, E., Beggan, C. D., Amit, H., Aubert, J., Baerenzung, J., ... Zhou, B. (2021, February). International Geomagnetic Reference Field: the thirteenth generation. *Earth, Planets and Space*, *73*(1), 49. Retrieved 2024-01-17, from `https://doi.org/10.1186/s40623-020-01288-x` doi: 10.1186/s40623-020-01288-x

Basu, S., & Basu, S. (1985). Equatorial scintillations: Advances since ISEA-6. *Journal of atmospheric and terrestrial physics*, *47*(8-10), 753–768. (Publisher: Elsevier)

Borovsky, J. E. (2012). Looking for evidence of mixing in the solar wind from 0.31 to 0.98 AU. *Journal of Geophysical Research: Space Physics*, *117*(A6). Retrieved 2022-04-29, from `http://onlinelibrary.wiley.com/doi/abs/10.1029/2012JA017525` (_eprint: https://agupubs.onlinelibrary.wiley.com/doi/pdf/10.1029/2012JA017525) doi: 10.1029/2012JA017525

Dyson, P. L., McClure, J. P., & Hanson, W. B. (1974, April). In situ measurements of the spectral characteristics of F region ionospheric irregularities. *Journal of Geophysical Research*, *79*(10), 1497–1502. Retrieved 2018-10-01, from `https://agupubs.onlinelibrary.wiley.com/doi/abs/10.1029/JA079i010p01497` doi: 10.1029/JA079i010p01497

Eccles, J. V., St. Maurice, J. P., & Schunk, R. W. (2015). Mechanisms underlying the prereversal enhancement of the vertical plasma drift in the low-latitude ionosphere. *Journal of Geophysical Research: Space Physics*, *120*(6), 4950–4970. Retrieved 2024-02-12, from `https://onlinelibrary.wiley.com/doi/abs/10.1002/2014JA020664` (_eprint: https://agupubs.onlinelibrary.wiley.com/doi/pdf/10.1002/2014JA020664) doi: 10.1002/2014JA020664

Fejer, B. G., Farley, D. T., Gonzales, C. A., Woodman, R. F., & Calderon, C. (1981). F region east-west drifts at Jicamarca. *Journal of Geophysical Re-*

search: Space Physics, *86*(A1), 215–218. Retrieved 2022-06-29, from http://onlinelibrary.wiley.com/doi/abs/10.1029/JA086iA01p00215 (_eprint: https://agupubs.onlinelibrary.wiley.com/doi/pdf/10.1029/JA086iA01p00215) doi: 10.1029/JA086iA01p00215

Friis-Christensen, E., Lühr, H., & Hulot, G. (2006, April). Swarm: A constellation to study the Earth's magnetic field. *Earth, Planets and Space*, *58*, BF03351933. doi: 10.1186/BF03351933

Hapgood, M. A. (1992, May). Space physics coordinate transformations: A user guide. *Planetary and Space Science*, *40*(5), 711–717. Retrieved 2024-01-17, from https://www.sciencedirect.com/science/article/pii/003206339290012D doi: 10.1016/0032-0633(92)90012-D

Heelis, R. A. (2004, July). Electrodynamics in the low and middle latitude ionosphere: a tutorial. *Journal of Atmospheric and Solar-Terrestrial Physics*, *66*(10), 825–838. Retrieved 2020-10-06, from http://www.sciencedirect.com/science/article/pii/S1364682604000525 doi: 10.1016/j.jastp.2004.01.034

Hysell, D. L., & Kelley, M. C. (1997). Decaying equatorial F region plasma depletions. *Journal of Geophysical Research: Space Physics*, *102*(A9), 20007–20017. Retrieved 2021-01-30, from http://agupubs.onlinelibrary.wiley.com/doi/abs/10.1029/97JA01725 (_eprint: https://onlinelibrary.wiley.com/doi/pdf/10.1029/97JA01725) doi: https://doi.org/10.1029/97JA01725

Hysell, D. L., & Kudeki, E. (2004). Collisional shear instability in the equatorial F region ionosphere. *Journal of Geophysical Research: Space Physics*, *109*(A11). Retrieved 2020-10-06, from https://agupubs.onlinelibrary.wiley.com/doi/abs/10.1029/2004JA010636 (_eprint: https://agupubs.onlinelibrary.wiley.com/doi/pdf/10.1029/2004JA010636) doi: 10.1029/2004JA010636

Hysell, D. L., Seyler, C. E., & Kelley, M. C. (1994). Steepened structures in equatorial spread F: 2. Theory. *Journal of Geophysical Research: Space Physics*, *99*(A5), 8841–8850. Retrieved 2021-01-30, from http://agupubs.onlinelibrary.wiley.com/doi/abs/10.1029/93JA02960 (_eprint: https://onlinelibrary.wiley.com/doi/pdf/10.1029/93JA02960) doi: https://doi.org/10.1029/93JA02960

Ivarsen, M. F., Jin, Y., Spicher, A., & Clausen, L. B. N. (2019). Direct Evidence for the Dissipation of Small-Scale Ionospheric Plasma Structures by a Conductive E Region. *Journal of Geophysical Research: Space Physics*, *124*(4), 2935–2942. Retrieved 2019-09-12, from https://agupubs.onlinelibrary.wiley.com/doi/abs/10.1029/2019JA026500 doi: 10.1029/2019JA026500

Ivarsen, M. F., Jin, Y., Spicher, A., Miloch, W., & Clausen, L. B. N. (2021). The Lifetimes of Plasma Structures at High Latitudes. *Journal of Geophysical Research: Space Physics*, *126*(2), e2020JA028117. Retrieved 2021-02-09, from http://agupubs.onlinelibrary.wiley.com/doi/abs/10.1029/2020JA028117 (_eprint: https://onlinelibrary.wiley.com/doi/pdf/10.1029/2020JA028117) doi: https://doi.org/10.1029/2020JA028117

Ivarsen, M. F., St-Maurice, J.-P., Jin, Y., Park, J., Miloch, W., Spicher, A., … Clausen, L. B. N. (2021). Steepening Plasma Density Spectra in the Ionosphere: The Crucial Role Played by a Strong E-Region. *Journal of Geophysical Research: Space Physics*, *126*(8), e2021JA029401. Retrieved 2021-08-18, from http://agupubs.onlinelibrary.wiley.com/doi/abs/10.1029/2021JA029401 (_eprint: https://onlinelibrary.wiley.com/doi/pdf/10.1029/2021JA029401) doi: 10.1029/2021JA029401

Kelley, M. C. (1989, January). Chapter 7 - Effects of Plasma Flow at High Latitudes. In M. C. Kelley (Ed.), *The Earth's Ionosphere* (pp. 311–343). Academic Press. Retrieved 2021-06-29, from https://www.sciencedirect.com/science/article/pii/B9780124040137500125 doi: 10.1016/B978-0-12-404013-7.50012-5

Kelley, M. C., Makela, J. J., Paxton, L. J., Kamalabadi, F., Comberiate, J. M., & Kil, H. (2003). The first coordinated ground- and space-based optical observations of equatorial plasma bubbles. *Geophysical Research Letters*, *30*(14). Retrieved 2022-07-15, from http://onlinelibrary.wiley.com/doi/abs/10.1029/2003GL017301 (_eprint: https://agupubs.onlinelibrary.wiley.com/doi/pdf/10.1029/2003GL017301) doi: 10.1029/2003GL017301

Kelley, M. C., & McClure, J. P. (1981, May). Equatorial spread-F: a review of recent experimental results. *Journal of Atmospheric and Terrestrial Physics*, *43*(5), 427–435. Retrieved 2020-10-06, from http://www.sciencedirect.com/science/article/pii/0021916981901069 doi: 10.1016/0021-9169(81)90106-9

Kelley, M. C., Pfaff, R., Baker, K. D., Ulwick, J. C., Livingston, R., Rino, C., & Tsunoda, R. (1982). Simultaneous rocket probe and radar measurements of equatorial spread F—Transitional and short wavelength results. *Journal of Geophysical Research: Space Physics*, *87*(A3), 1575–1588.

Kil, H. (2015). The Morphology of Equatorial Plasma Bubbles - a review. *Journal of Astronomy and Space Sciences*, *32*(1), 13–19. Retrieved 2020-10-06, from http://koreascience.or.kr/article/JAKO201509956027427.page (Publisher: The Korean Space Science Society) doi: 10.5140/JASS.2015.32.1.13

Kil, H., & Heelis, R. A. (1998). Equatorial density irregularity structures at intermediate scales and their temporal evolution. *Journal of Geophysical Research: Space Physics*, *103*(A3), 3969–3981. Retrieved 2020-10-06, from https://agupubs.onlinelibrary.wiley.com/doi/abs/10.1029/97JA03344 (_eprint: https://agupubs.onlinelibrary.wiley.com/doi/pdf/10.1029/97JA03344) doi: 10.1029/97JA03344

Kivanc, & Heelis, R. A. (1998, April). Spatial distribution of ionospheric plasma and field structures in the high-latitude F region. *Journal of Geophysical Research*, *103*, 6955–6968. Retrieved 2018-08-13, from http://adsabs.harvard.edu/abs/1998JGR...103.6955K doi: 10.1029/97JA03237

Knudsen, D. J., Burchill, J. K., Buchert, S. C., Eriksson, A. I., Gill, R., Wahlund, J.-E., … Moffat, B. (2017, February). Thermal ion imagers and Langmuir probes in the Swarm electric field instruments. *Journal of Geophysical Research: Space Physics*, *122*(2), 2016JA022571. Retrieved 2018-03-07, from http://onlinelibrary.wiley.com/doi/10.1002/2016JA022571/abstract doi: 10.1002/2016JA022571

Kolmogorov, A. (1941). The Local Structure of Turbulence in Incompressible Viscous Fluid for Very Large Reynolds' Numbers. *Akademiia Nauk SSSR Doklady*, *30*, 301–305. Retrieved 2018-05-08, from http://adsabs.harvard.edu/abs/1941DoSSR..30..301K

LaBelle, J., Kelley, M. C., & Seyler, C. E. (1986). An analysis of the role of drift waves in equatorial spread F. *Journal of Geophysical Research: Space Physics*, *91*(A5), 5513–5525. (Publisher: Wiley Online Library)

Le, G., Huang, C.-S., Pfaff, R. F., Su, S.-Y., Yeh, H.-C., Heelis, R. A., … Hairston, M. (2003). Plasma density enhancements associated with equatorial spread F: ROCSAT-1 and DMSP observations. *Journal of Geophysical Research: Space Physics*, *108*(A8). Retrieved 2020-10-06, from https://agupubs.onlinelibrary.wiley.com/doi/abs/10.1029/2002JA009592 (_eprint: https://agupubs.onlinelibrary.wiley.com/doi/pdf/10.1029/2002JA009592) doi: 10.1029/2002JA009592

Moisan, M., & Pelletier, J. (2012). Hydrodynamic Description of a Plasma. In

M. Moisan & J. Pelletier (Eds.), *Physics of Collisional Plasmas: Introduction to High-Frequency Discharges* (pp. 203–335). Dordrecht: Springer Netherlands. Retrieved 2019-09-02, from https://doi.org/10.1007/978-94-007-4558-2_3 doi: 10.1007/978-94-007-4558-2_3

Mounir, H., Berthelier, A., Cerisier, J. C., Lagoutte, D., & Beghin, C. (1991, November). The small-scale turbulent structure of the high latitude ionosphere - Arcad-Aureol-3 observations. *Annales Geophysicae*, *9*, 725–737. Retrieved 2018-03-07, from http://adsabs.harvard.edu/abs/1991AnGeo...9..725M

Nakanishi, K., Iyemori, T., Taira, K., & Lühr, H. (2014, May). Global and frequent appearance of small spatial scale field-aligned currents possibly driven by the lower atmospheric phenomena as observed by the CHAMP satellite in middle and low latitudes. *Earth, Planets and Space*, *66*(1), 40. Retrieved 2022-06-30, from https://doi.org/10.1186/1880-5981-66-40 doi: 10.1186/1880-5981-66-40

Oya, H., Takahashi, T., & Watanabe, S. (1986). Observation of Low Latitude Ionosphere by the Impedance Probe on Board the Hinotori Satellite. *Journal of geomagnetism and geoelectricity*, *38*(2), 111–123. doi: 10.5636/jgg.38.111

Park, J., Min, K. W., Lee, J.-J., Kil, H., Kim, V. P., Kim, H.-J., … Lee, D. Y. (2003). Plasma blob events observed by KOMPSAT-1 and DMSP F15 in the low latitude nighttime upper ionosphere. *Geophysical Research Letters*, *30*(21). Retrieved 2020-10-06, from https://agupubs.onlinelibrary.wiley.com/doi/abs/10.1029/2003GL018249 (_eprint: https://agupubs.onlinelibrary.wiley.com/doi/pdf/10.1029/2003GL018249) doi: 10.1029/2003GL018249

Purslow, B. W. (1958, January). Ionospheric Drift in the F2 Region near the Magnetic Equator. *Nature*, *181*(4601), 35–36. Retrieved 2022-06-29, from http://www.nature.com/articles/181035a0 (Number: 4601 Publisher: Nature Publishing Group) doi: 10.1038/181035a0

Rino, C. L., Carrano, C. S., Groves, K. M., & Roddy, P. A. (2016). A characterization of intermediate-scale spread F structure from four years of high-resolution C/NOFS satellite data. *Radio Science*, *51*(6), 779–788. (Publisher: AGU)

Rino, C. L., Tsunoda, R. T., Petriceks, J., Livingston, R. C., Kelley, M. C., & Baker, K. D. (1981). Simultaneous rocket-borne beacon and in situ measurements of equatorial spread F—Intermediate wavelength results. *Journal of Geophysical Research: Space Physics*, *86*(A4), 2411–2420. Retrieved 2020-10-06, from https://agupubs.onlinelibrary.wiley.com/doi/abs/10.1029/JA086iA04p02411 (_eprint: https://agupubs.onlinelibrary.wiley.com/doi/pdf/10.1029/JA086iA04p02411) doi: 10.1029/JA086iA04p02411

Skinner, N. J., Hope, J., & Wright, R. W. (1958, November). Horizontal Drift Measurements in the Ionosphere near the Equator. *Nature*, *182*(4646), 1363–1365. Retrieved 2022-06-29, from http://www.nature.com/articles/1821363a0 (Number: 4646 Publisher: Nature Publishing Group) doi: 10.1038/1821363a0

Song, H., Park, J., Buchert, S., Jin, Y., Chao, C. K., Lee, J., & Yi, Y. (2022). A Small Peak in the Swarm-LP Plasma Density Data at the Dayside Dip Equator. *Journal of Geophysical Research: Space Physics*, *127*(7), e2022JA030319. Retrieved 2024-01-05, from https://onlinelibrary.wiley.com/doi/abs/10.1029/2022JA030319 (_eprint: https://onlinelibrary.wiley.com/doi/pdf/10.1029/2022JA030319) doi: 10.1029/2022JA030319

Stoica, P., & Moses, R. L. (2005). *Spectral Analysis of Signals*. Pearson Prentice Hall. (Google-Books-ID: h78ZAQAAIAAJ)

Su, S.-Y., Liu, C. H., Ho, H. H., & Chao, C. K. (2006). Distribution characteristics of topside ionospheric density irregularities: Equatorial versus midlatitude regions. *Journal of Geophysical Research:*

Space Physics, *111*(A6). Retrieved 2024-03-07, from https://onlinelibrary.wiley.com/doi/abs/10.1029/2005JA011330 (_eprint: https://agupubs.onlinelibrary.wiley.com/doi/pdf/10.1029/2005JA011330) doi: 10.1029/2005JA011330

Tröbs, M., & Heinzel, G. (2006, February). Improved spectrum estimation from digitized time series on a logarithmic frequency axis. *Measurement*, *39*(2), 120–129. Retrieved 2018-03-06, from http://www.sciencedirect.com/science/article/pii/S026322410500117X doi: 10.1016/j.measurement.2005.10.010

Vickrey, J. F., & Kelley, M. C. (1982, June). The effects of a conducting E layer on classical F region cross-field plasma diffusion. *Journal of Geophysical Research: Space Physics*, *87*(A6), 4461–4468. Retrieved 2018-03-06, from http://onlinelibrary.wiley.com/doi/10.1029/JA087iA06p04461/abstract doi: 10.1029/JA087iA06p04461

Woodman, R. F. (1972). East-west ionospheric drifts at the magnetic equator. *undefined*. Retrieved 2022-06-29, from https://www.semanticscholar.org/paper/East-west-ionospheric-drifts-at-the-magnetic-Woodman/5c3b012a8a68019199019ca2f8d7452e7d9fd74c

Woodman, R. F., & Hoz, C. L. (1976). Radar observations of F region equatorial irregularities. *Journal of Geophysical Research (1896-1977)*, *81*(31), 5447–5466. Retrieved 2020-10-06, from https://agupubs.onlinelibrary.wiley.com/doi/abs/10.1029/JA081i031p05447 (_eprint: https://agupubs.onlinelibrary.wiley.com/doi/pdf/10.1029/JA081i031p05447) doi: 10.1029/JA081i031p05447

Yeh, K. C., & Liu, C.-H. (1982, April). Radio wave scintillations in the ionosphere. *IEEE Proceedings*, *70*, 324–360. Retrieved 2018-05-08, from http://adsabs.harvard.edu/abs/1982IEEEP..70..324Y